

Contents

1	Introduction and Theory Overview	1
1.1	Introduction	1
1.2	Theory Overview	2
1.2.1	Heavy Vector Triplet Model	2
1.2.2	Basic Phenomenology	3
1.2.3	Explicit Models	8
2	CMS detector and LHC	11
2.1	Large Hadron Collider	11
2.2	Compact Muon Solenoid	13
2.2.1	Tracker	15
2.2.2	ECAL	16
2.2.3	HCAL	17
2.2.4	Muon Chamber	19
2.2.5	Trigger System	20
3	Analysis Procedures	22
3.1	Monte Carlo Samples and Data sets	22
3.1.1	Signal MC	22

List of Figures

1-1	Branching ratios as a function of the resonance mass for the HVT benchmark model A(left) and model B(right).	10
1-2	Theoretical production cross-section as a function of new resonance particles for HVT model B benchmark. Dash lines are 8 TeV predictions while solid lines are 13 TeV predictions.	10
2-1	Overview of the LHC and relative location of the detectors.	12
2-2	CERN accelerator complex.	13
2-3	Structure overview of the CMS detector.	14
2-4	Schematic layout of tracker.	15
2-5	The pixel detector inside tracker.	15
2-6	Schematic layout of the CMS ECAL.	17
2-7	Longitudinal view of one quarter of CMS and the location of HB (hadron barrel calorimeter), HE (hadron endcap calorimeter), HF (hadron forward calorimeter) and HO (hadron outer calorimeter)	18
2-8	Slice view of one quarter of muon chamber system.	20
2-9	CMS triggering and data acquisition architecture.	21

List of Tables

3.1 Signal samples used in the analysis.	23
--	----

¹ Chapter 1

² Introduction and Theory Overview

³ 1.1 Introduction

⁴ This thesis presents the analysis details and the results of the search for heavy reso-
⁵ nances decaying into a Z boson and a Higgs boson (h) at the center-of-mass energy of
⁶ 8 TeV, using 19.7 fb^{-1} p-p collision data. In turn, the Z boson is identified through
⁷ its leptonic decays (leptons often refer to e and μ only in experiments. $l = e, \mu$). The
⁸ Higgs boson h is expected to hadronically decay into a pair of b-quarks. The investi-
⁹ gated final states consist of two charged leptons which are identified in the detector
¹⁰ and limit the presence of the background, and two b-quarks from the hadronic Higgs
¹¹ decay which collects the largest possible fraction of Higgs events.

¹² This thesis is organised as follows. In the latter part of this chapter, the model that
¹³ predicts heavy resonances is introduced, including the expected cross section and the
¹⁴ specification of model parameters. In chapter 2, the LHC and the CMS experiment
¹⁵ are described, including the information of each sub-detector and the trigger system
¹⁶ of the CMS. The details of the analysis are shown in chapter 3. This chapter reveals
¹⁷ the way to reconstruct physical objects in CMS. By adding some proper kinematic
¹⁸ selections on those physics objects, the interested events in data collected by the CMS
¹⁹ detector can be selected. Moreover, this chapter shows the comparison between data
²⁰ and simulation. In the last chapter, the results of the search and the conclusion are
²¹ presented.

22 1.2 Theory Overview

23 Although the Higgs boson discovered by the ATLAS and CMS collaborations [1–3]
 24 imposes strong constraints on theories beyond the Standard Model(SM), the extreme
 25 fine tuning in quantum corrections required to have a light fundamental Higgs boson
 26 with mass close to 125 GeV [4–7] suggests that the Standard Model may be incom-
 27 plete, and not valid beyond a scale of a few TeV. Various dynamical electroweak
 28 symmetry breaking scenarios which attempt to solve this naturalness problem, such
 29 as Minimal Walking Technicolor [8], Little Higgs [9–11], or composite Higgs mod-
 30 els [12–14] predict the existence of new resonances decaying to a vector boson plus a
 31 Higgs boson.

32 1.2.1 Heavy Vector Triplet Model

33 Resonance searches are typically not sensitive to all the details and the free parameters
 34 of the underlying model, but only to those parameters or combinations of parameters
 35 that control the mass of the resonance and the interactions involved in its production
 36 and decay. Therefore, one can employ a simplified description of the resonance de-
 37 fined by a phenomenological Lagrangian where only the relevant couplings and mass
 38 parameters are retained. This model-independent strategy applies a Heavy Vector
 39 Triplet (HVT) [15] to the Standard Model group and reproduces a large class of ex-
 40 plicit models. In Eq. (1.1), the mathematical form of the simplified Lagrangian is
 41 defined, where V_ν^a , $a = 1,2,3$, is a real vector with vanishing hypercharge in the ad-
 42 joint representation of $SU(2)_L$, it describes one charged and one neutral heavy spin-1
 43 particle with charge eigenstate fields, and $D_{[\mu} V_{\nu]}^a$ represents the covariant derivative.

$$\begin{aligned} \mathcal{L}_V = & -\frac{1}{4} D_{[\mu} V_{\nu]}^a D^{[\mu} V^{\nu]}_a + \frac{m_V^2}{2} V_\mu^a V^{\mu a} \\ & + ig_V c_H V_\mu^a H^\dagger \tau^a \overset{\leftrightarrow}{D}^\mu H + \frac{g^2}{g_V} c_F V_\mu^a \sum_f \bar{f}_L \gamma^\mu \tau^a f_L \\ & + \frac{g_V}{2} c_{VVV} \epsilon_{abc} V_\mu^a V_\nu^b D^{[\mu} V^{\nu]}_c + \text{quadrilinear terms} \end{aligned} \quad (1.1)$$

$$V_\mu^\pm = \frac{V_\mu^1 \mp i V_\mu^2}{\sqrt{2}}, \quad V_\mu^0 = V_\mu^3 \quad (1.2)$$

$$D_{[\mu} V_{\nu]}^a = D_\mu V_\nu^a - D_\nu V_\mu^a, \quad D_\mu V_\nu^a = \partial_\mu V_\nu^a + g \epsilon^{abc} W_\mu^b V_\nu^c \quad (1.3)$$

$$H = \begin{pmatrix} \phi^+ \\ \phi^- \end{pmatrix} = \begin{pmatrix} \frac{1}{\sqrt{2}}(\phi_1 + i\phi_2) \\ \frac{1}{\sqrt{2}}(\phi_3 + i\phi_4) \end{pmatrix} \quad (1.4)$$

⁴⁴

⁴⁵ In these models, new heavy vector bosons (V^\pm, V^0) that couple to the SM Higgs
⁴⁶ doublet (Eq. 1.4) and SM gauge bosons with the parameters c_H and g_V and to the
⁴⁷ fermions via the combination $(g^2/g_V)c_F$. The parameter g_V represents the strength
⁴⁸ of the new vector boson interaction, while c_H and c_F represent the couplings to the
⁴⁹ Higgs and the fermions respectively, and are expected to be of the order of unity in
⁵⁰ most models.

⁵¹ 1.2.2 Basic Phenomenology

⁵² Masses and Mixings

After electro-weak symmetry breaking (EWSB), the only massless state is photon, which can be identified as the gauge field associated with the unbroken $U(1)_{em}$. The two other neutral mass eigenstates are the SM Z boson and one heavy vector of mass M_0 which are obtained by diagonalizing the mass matrix of the (Z, V^0) system by a rotation with angle θ_N

$$\begin{pmatrix} Z \\ V^0 \end{pmatrix} \rightarrow \begin{pmatrix} \cos \theta_N & \sin \theta_N \\ -\sin \theta_N & \cos \theta_N \end{pmatrix} \begin{pmatrix} Z \\ V^0 \end{pmatrix}. \quad (1.5)$$

The mass matrix is

$$\mathcal{M}_N^2 = \begin{pmatrix} \hat{m}_Z^2 & c_H \xi \hat{m}_Z \hat{m}_V \\ c_H \xi \hat{m}_Z \hat{m}_V & \hat{m}_V^2 \end{pmatrix}, \text{ where } \begin{cases} \hat{m}_Z = \frac{e\hat{v}}{2\sin\theta_W \cos\theta_W} \\ \hat{m}_V^2 = m_V^2 + g_V^2 c_{VVHH} \hat{v}^2 \\ \xi = \frac{g_V \hat{v}}{2\hat{m}_V} \end{cases}. \quad (1.6)$$

In the above equations \hat{v} denotes the Vacuum Expectation Value (VEV) defined by $\langle H^\dagger H \rangle = \hat{v}^2/2$, and one should know the masses \hat{m}_Z and \hat{m}_V do not coincide with the physical Z boson and the masses of the new resonances of this model, although they do in the approximations later. The mass eigenvalues and the rotation angles are easily obtained by inverting the relations

$$\begin{aligned} Tr[\mathcal{M}_N^2] &= \hat{m}_Z^2 + \hat{m}_V^2 = m_Z^2 + M_0^2, \\ Det[\mathcal{M}_N^2] &= \hat{m}_Z^2 \hat{m}_V^2 (1 - c_H^2 \xi^2) = m_Z^2 M_0^2, \\ \tan 2\theta_N &= \frac{2c_H \xi \hat{m}_Z \hat{m}_V}{\hat{m}_V^2 - \hat{m}_Z^2}. \end{aligned} \quad (1.7)$$

⁵³ Notice that the tangent can be uniquely inverted because the angle θ_N is in the range

⁵⁴ $[-\pi/4, \pi/4]$ in the parameter region we will be interested in, where $\hat{m}_Z < \hat{m}_V$, and

⁵⁵ M_0 represents the real mass eigenvalue of the neutral heavy vector boson.

The situation is similar in the charged vector mass matrix of (W^\pm, V^\pm) system, and M_\pm denotes the real mass eigenvalue of charged states as well.

$$\mathcal{M}_C^2 = \begin{pmatrix} \hat{m}_W^2 & c_H \xi \hat{m}_W \hat{m}_V \\ c_H \xi \hat{m}_W \hat{m}_V & \hat{m}_V^2 \end{pmatrix}, \text{ where } \hat{m}_W = \frac{e\hat{v}}{2\sin\theta_W} = \cos\theta_W \hat{m}_Z, \quad (1.8)$$

where it is diagonalized by

$$\begin{aligned} Tr[\mathcal{M}_C^2] &= \hat{m}_W^2 + \hat{m}_V^2 = m_W^2 + M_\pm^2, \\ Det[\mathcal{M}_C^2] &= \hat{m}_W^2 \hat{m}_V^2 (1 - c_H^2 \xi^2) = m_W^2 M_\pm^2, \\ \tan 2\theta_C &= \frac{2c_H \xi \hat{m}_W \hat{m}_V}{\hat{m}_V^2 - \hat{m}_W^2}. \end{aligned} \quad (1.9)$$

By checking Eq. (1.6) and Eq. (1.8), the charged and neutral mass matrices are connected by custodial symmetry, which can be shown in full generality to imply

$$\mathcal{M}_C^2 = \begin{pmatrix} \cos \theta_W & 0 \\ 0 & 1 \end{pmatrix} \mathcal{M}_N^2 \begin{pmatrix} \cos \theta_W & 0 \\ 0 & 1 \end{pmatrix}. \quad (1.10)$$

By taking the determinant of the above equation, or equivalently by comparing the charged and neutral determinants in Eq. (1.7) and Eq. (1.9), we obtain a generalized custodial relation among the physical masses

$$m_W^2 M_{\pm}^2 = \cos^2 \theta_W m_Z^2 M_0^2. \quad (1.11)$$

From the simple formula above, we can start to identify the physically reasonable region of the parameter space in this model. We aim at describing new vectors with masses at or above the TeV scale, but we also want the SM masses $m_{W,Z} \sim 100$ GeV to be reproduced. Therefore we require a hierarchy in the mass relation of SM Z and W bosons versus the new vectors.

$$\frac{\hat{m}_{W,Z}}{\hat{m}_V} \sim \frac{m_{W,Z}}{M_{\pm,0}} \leq 10^{-1} \ll 1 \quad (1.12)$$

In the limit of Eq. (1.12) we obtain simple approximation for m_W and m_Z

$$\begin{aligned} m_Z^2 &= \hat{m}_Z^2 (1 - c_H^2 \xi^2) (1 + \mathcal{O}(\hat{m}_Z^2 / \hat{m}_V^2)), \\ m_W^2 &= \hat{m}_W^2 (1 - c_H^2 \xi^2) (1 + \mathcal{O}(\hat{m}_W^2 / \hat{m}_V^2)). \end{aligned} \quad (1.13)$$

The parameter ξ can be either very small or of order unity. Both cases are realized in explicit models. While $\xi \ll 1$ is the most common situation, $\xi \sim 1$ only occurs in strongly coupled scenarios at very large g_V . In these approximations, SM tree-level experimental observation can be reproduced to percent accuracy.

Since $\hat{m}_W = \cos \theta_W \hat{m}_Z$, the W - Z mass ratio is thus given by

$$\frac{m_W^2}{m_Z^2} \simeq \cos^2 \theta_W . \quad (1.14)$$

Eq. (1.14) has one important implication on the masses of the new vectors. When combined with the custodial relation Eq. (1.11), it tells us that the charged and neutral V s are practically degenerate

$$M_{\pm}^2 = M_0^2(1 + \mathcal{O}(\%)) , \quad (1.15)$$

⁵⁶ In the following, when working at the leading order in the limit Eq. (1.12), we can
⁵⁷ ignore the mass splitting and denote the mass of the charged and the neutral states
⁵⁸ collectively as M_V . It is easy to check that in that limit $M_V = \hat{m}_V$.

⁵⁹ Decay Widths

Because of the hierarchy in the mass matrices, the mixing angles are naturally small. By looking at Eqs. (1.7), (1.9) and (1.12) we can estimate

$$\theta_{N,C} \simeq c_H \xi \frac{\hat{m}_{W,Z}}{\hat{m}_V} \leq 10^{-1} , \quad (1.16)$$

and after rotating to the mass basis, the coupling of the neutral and charged resonances to left- and right-handed fermion chiralities can be written in a compact form for each fermion species $F = \{l, q, 3\}$.

$$\begin{cases} g_L^N = \frac{g^2}{g_V} \frac{c_F}{2} \cos \theta_C + (g_L^Z)_{SM} \sin \theta_N \simeq \frac{g^2}{g_V} \frac{c_F}{2} , \\ g_R^N = (g_R^Z)_{SM} \sin \theta_N \simeq 0 \\ g_L^C = \frac{g^2}{g_V} \frac{c_F}{2} \cos \theta_C + (g_L^W)_{SM} \sin \theta_C \simeq \frac{g^2}{g_V} \frac{c_F}{2} , \\ g_R^C = 0 \end{cases} \quad (1.17)$$

In the above equation $(g_{L,R}^{W,Z})_{SM}$ denote the ordinary SM W and Z couplings (with the normalization given by $g_L^W = g/\sqrt{2}$).

Given that the rotation angles are small, the couplings further simplify, as also shown in the equation. We could see that V interact mainly with left-handed chiralities and that all the couplings for each fermion species are controlled by the parameter combination g^2/g_{VC_F} . This gives tight correlations among different channels

$$\Gamma_{V_\pm \rightarrow f\bar{f}'} \simeq 2\Gamma_{V_0 \rightarrow f\bar{f}'} \simeq N_C[f] \left(\frac{g^2 c_F}{g_V}\right)^2 \frac{M_V}{48\pi}, \quad (1.18)$$

where $N_C[f]$ is the number of colors (3 for the di-quark and 1 for the dilepton decays). The parameters $c_F = \{c_l, c_q, c_3\}$ control the relative BRs to leptons, light quarks and the third family.

In the case of di-boson decay width

$$\begin{aligned} \Gamma_{V_0 \rightarrow W_L^+ W_L^-} &\simeq \Gamma_{V_\pm \rightarrow W_L^\pm Z_L} \simeq \frac{g_V^2 c_H^2 M_V}{192\pi} \frac{(1 + c_H c_{VVV} \xi^2)^2}{(1 - c_H^2 \xi^2)^2} = \frac{g_V^2 c_H^2 M_V}{192\pi} [1 + \mathcal{O}(\xi^2)], \\ \Gamma_{V_0 \rightarrow Z_L h} &\simeq \Gamma_{V_\pm \rightarrow W_L^\pm h} \simeq \frac{g_V^2 c_H^2 M_V}{192\pi} \frac{(1 - 4c_{VVHH} \xi^2)^2}{1 - c_H^2 \xi^2} = \frac{g_V^2 c_H^2 M_V}{192\pi} [1 + \mathcal{O}(\xi^2)]. \end{aligned} \quad (1.19)$$

⁶⁰ Note that Eq. (1.19) is derived in the Equivalent Gauge [16] because the decay to transverse SM vectors is highly suppressed while to the longitudinal parts grows with the energy of the process, therefore the Unitary Gauge which is used in the original Lagrangian is instead useful. The channels that are not shown in the above equations are either forbidden or suppressed like the decays to transverse polarizations.

⁶⁵ From this section, a very simple picture emerges. At small ξ , all the decay widths are fixed with a given resonance mass M_V and the couplings $\{g^2 c_F/g_V, g_{VC_H}\}$ which control the BRs in all relevant channels. Parameters c_{VVV} , c_{VVHH} and c_{VWW} are basically irrelevant. Thus, the basic phenomenology of this model is well described by a good approximation.

⁷⁰ 1.2.3 Explicit Models

Now the general picture is clear, we can get exact values of the widths and BRs from explicit models. Consider two benchmark models, A and B, which correspond to two explicit models describing the heavy vectors in Refs. [17] and [12] respectively. All the c parameters are fixed to specific values in these models and the only free parameters are the resonance mass M_V and coupling g_V . Moreover, model A is inspired by weakly coupled extensions of the SM gauge group while model B is by strongly coupled scenarios of EWSB, *i.e.* Composite Higgs models, we will consider them in different regions of g_V , relatively small $g_V \leq 3$ and relatively large $g_V \geq 3$.

Figure 1-1 shows the BRs as functions of the mass in model A and B. As expected from the previous discussion and according to Refs. [17], model A predicts

$$c_H = -g^2/g_V^2, c_F \simeq 1, \\ |g_V c_H| \simeq g^2 c_F / g_V \simeq g^2 / g_V. \quad (1.20)$$

Therefore Eq. (1.18) and (1.19) can be determined in the following form for V_0 in model A ($g_V = 1$),

$$\Gamma_{V_0 \rightarrow f\bar{f}'} \simeq N_c[f] \frac{g^4 M_V}{96\pi} \\ \Gamma_{V_0 \rightarrow W^+W^-} \simeq \Gamma_{V_0 \rightarrow Zh} \simeq \frac{g^4 M_V}{192\pi}. \quad (1.21)$$

One can easily check either from the plot or the equation, a factor of two difference comparing the BRs between fermions and bosons. Due to the color factor, leptons and quarks also have a difference by a factor of three. Since the c_F term is universal both in A and B. The total width in model A decreases with increasing g_V because of the overall suppression (g^2/g_V) in Eq. (1.20).

On the contrary, in model B the c_H term is unsuppressed

$$c_H \simeq c_F \simeq 1 , \\ g_V c_H \simeq -g_V , g^2 c_{c_F} / g_{g_V} \simeq g^2 / g_V . \quad (1.22)$$

Thus the determinate V_0 decay widths for model B ($g_V = 3$) are

$$\Gamma_{V_0 \rightarrow f\bar{f}'} \simeq N_c[f] \frac{g^4 M_V}{342\pi} \\ \Gamma_{V_0 \rightarrow W^+W^-} \simeq \Gamma_{V_0 \rightarrow Zh} \simeq \frac{3M_V}{64\pi} . \quad (1.23)$$

- ⁷¹ For model B _{$g_V=3$} the dominant BRs are into di-bosons and the fermionic decays are
- ⁷² extremely suppressed. Moreover, the total width increases with increasing g_V since it
- ⁷³ is dominated by the di-boson width which grows with g_V as expected from Eq. (1.22).
- ⁷⁴ This model B is particularly interesting for the present search, since it predicts signal
- ⁷⁵ cross sections in order of fb [15] [18] [Fig. 1-2], branching ratios to vector bosons close
- ⁷⁶ to unity, and thus being accessible at the LHC. In the latter chapters, the mass eigen-
- ⁷⁷ state of the neutral heavy vector boson in model B scenario refers to the Z' particle,
- ⁷⁸ which is the search target of this thesis.

⁷⁹

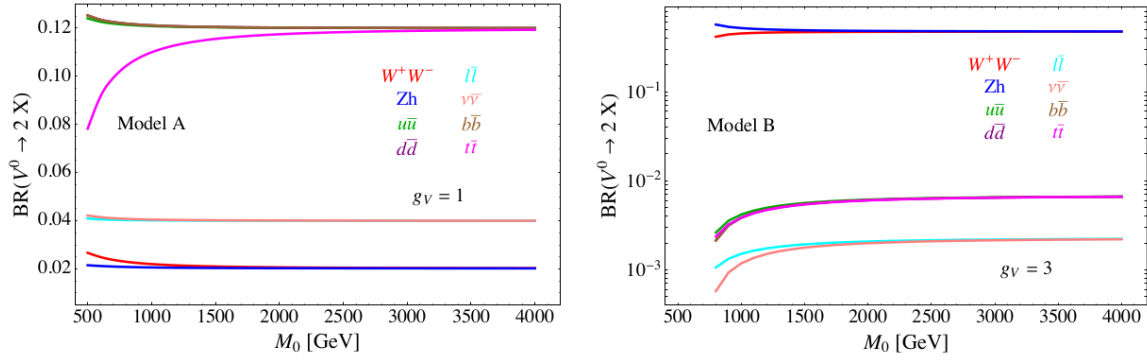


Figure 1-1: Branching ratios as a function of the resonance mass for the HVT benchmark model A(left) and model B(right).

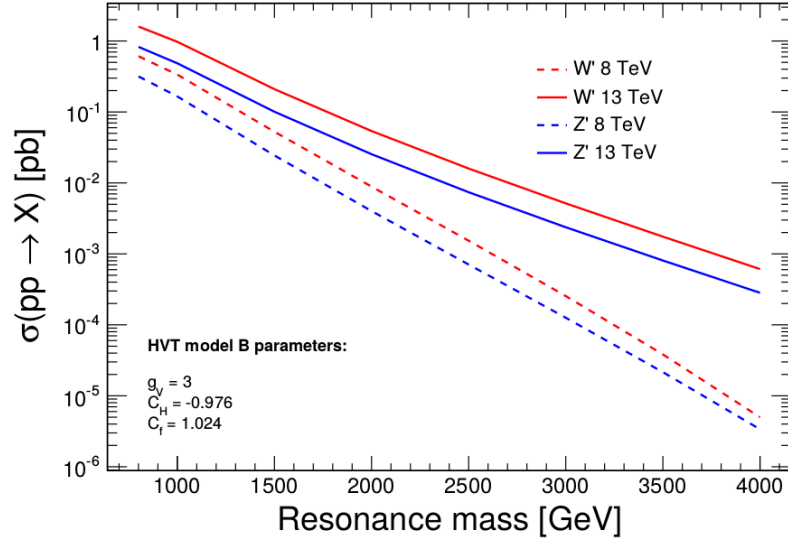


Figure 1-2: Theoretical production cross-section as a function of new resonance particles for HVT model B benchmark. Dash lines are 8 TeV predictions while solid lines are 13 TeV predictions.

80 **Chapter 2**

81 **CMS detector and LHC**

82 This thesis is done via analyzing the data collected by the Compact Muon Solenid
83 (CMS) detector at the Large Hadron Collider (LHC). CMS is one of the two largest
84 detectors built on the LHC. This chapter will briefly introduce the LHC and the CMS
85 detector.

86 **2.1 Large Hadron Collider**

87 The LHC is the world’s most powerful hadron collider and the largest experimental
88 facility ever. It was built by the European Organization for Nuclear Research (CERN)
89 between 1998 and 2008 in collaboration with over 10,000 scientists and engineers from
90 over 100 countries, as well as hundreds of universities and laboratories. It lies in a
91 tunnel 27 km in circumference, as deep as 175 m beneath the France–Switzerland
92 border near Geneva. The designed maximum collision energy and highest luminosity
93 of the LHC are 14 TeV and $10^{-34}\text{cm}^{-2}\text{s}^{-1}$ respectively.

94 Other accelerators that had been originally built at CERN for previous experiments
95 is working as an injection chain for the LHC now. The proton beam starts
96 from LINAC, a small linear accelerator, where its energy firstly reaches 50 MeV. It
97 then passes through a booster and goes to the PS, where it is accelerated up to 25
98 GeV. After that, it reaches 450 GeV in the SPS. The beam is finally injected in the
99 LHC ring from the SPS, it is accelerated up to 4 TeV in 2012. In early 2015, the

100 proton beam had been accelerated to 6.5 TeV, a value near its designed energy, before
101 undergoing collision.

102 There are four collision points at the LHC, corresponding to four main experiments, CMS, ATLAS, LHCb and ALICE. The ALICE experiment is optimized to
103 study heavy-ion (Pb-Pb nuclei) collisions and focusing on the physics of strongly
104 interacting matter at extreme energy densities. LHCb is a specialized b-physics ex-
105 periment, measuring the parameters of CP violation in the interactions of b-hadrons.
106 Such studies can help to explain the matter-antimatter asymmetry of the universe.
107 Last, CMS and ATLAS are two general purpose detectors. The aims of these two
108 experiments are investigating a wide range of physics, including the search for the
109 beyond standard model particles, extra dimensions, and dark matter.



Figure 2-1: Overview of the LHC and relative location of the detectors.

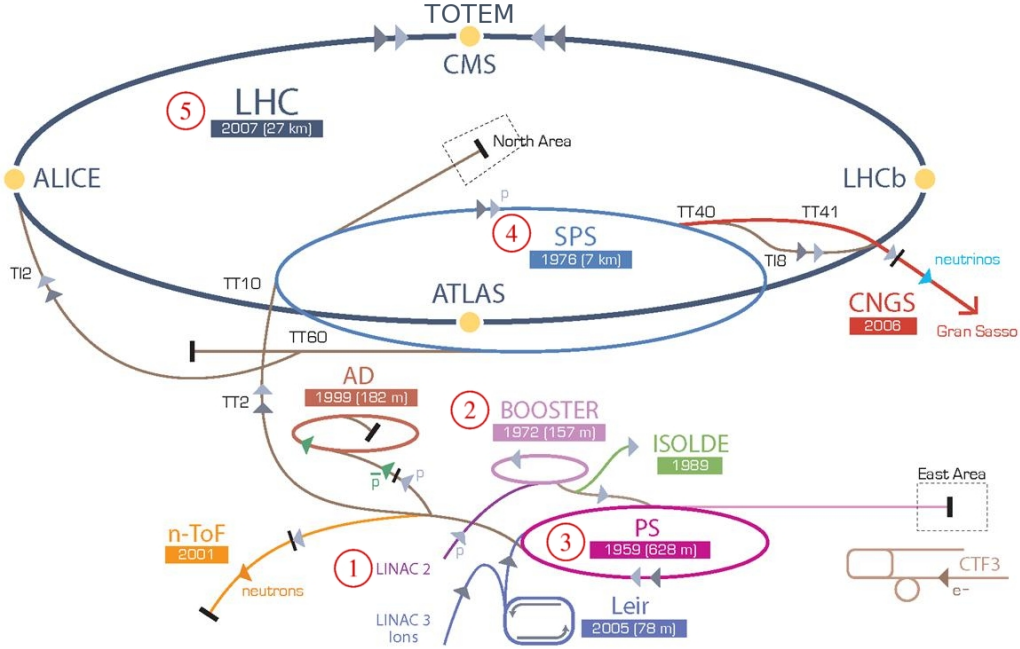


Figure 2-2: CERN accelerator complex.

2.2 Compact Muon Solenoid

The Compact Muon Solenoid (CMS) is designed to cope very high rate of interactions expected to take place at the high LHC luminosity. It has the typical structure of detectors at hadron colliders: a central region (*barrel*) enclosed by two disks (*endcaps*). The structure of CMS can be seen in Fig. (2-3).

Solenoid and Sub-detectors

CMS features a powerful superconducting coil, generating a solenoidal magnetic field around 3.8 Tesla in a large volume which hosts different sub-detectors. The magnetic field lines close through steel yoke in the outer region and the distinct sub-detectors are designed in order to obtain the highest possible resolution and the largest acceptance for every kind of particles.

The innermost layer is a silicon-based tracker. Surrounding it is a scintillating crystal electromagnetic calorimeter (ECAL), which is itself surrounded with a sampling calorimeter for hadrons (HCAL). The tracker and the calorimeters are compact

125 enough to fit inside the CMS Solenoid. Outside the magnet are the large muon
126 chambers.

CMS Detector

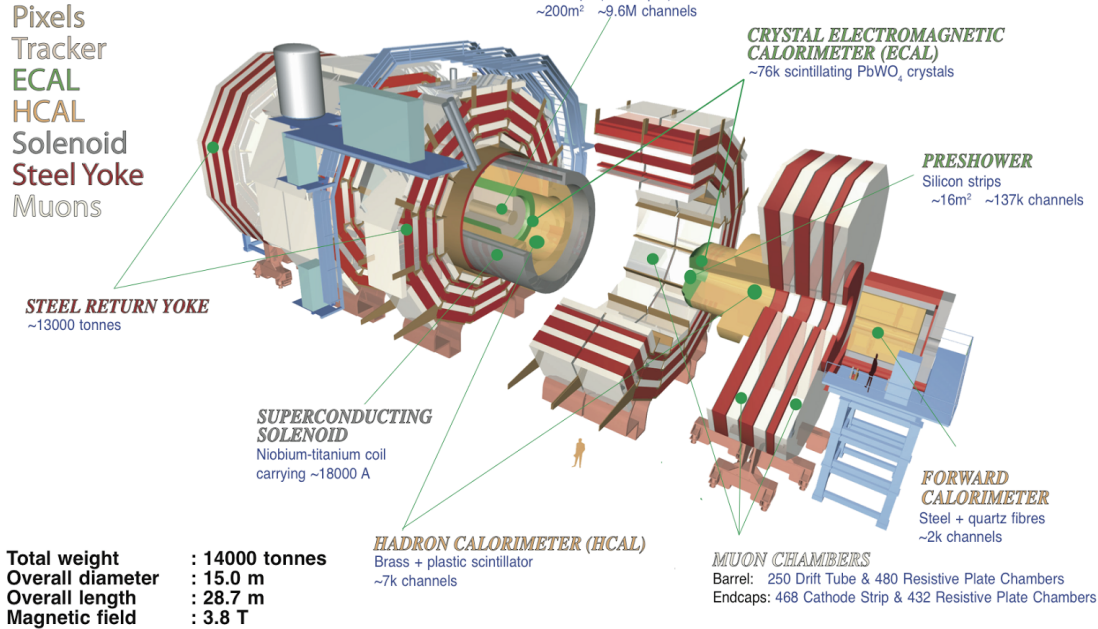


Figure 2-3: Structure overview of the CMS detector.

127 Coordinate System

128 The CMS coordinate system is oriented such that the x -axis points to the center of
129 the LHC ring, the y -axis points vertically upward and the z -axis is in the direction
130 of the beam. The azimuthal angle ϕ is measured from the x -axis in the $x - y$ plane
131 and the radial coordinate in this plane is denoted by r . The polar angle θ is defined
132 in the $r - z$ plane, while the pseudo-rapidity $\eta = -\ln \tan(\theta/2)$. The momentum
133 component transverse to the beam direction, denoted by p_T , is computed from the x -
134 and y -components, and the transverse energy is defined as $E_T = E \sin \theta$.

135 2.2.1 Tracker

136 Tracker is the most inner part of CMS that contacts the productions of collisions in
137 the first place. It traces the charged particles' trajectories without considering their
138 energy as possible. Physicists can reconstruct the vertices of the interaction and the
139 momentum of charged particles by linking tracks to the collider's pipe and measuring
140 the curves of particles under magnetic field.

141 The tracking system is composed of two kinds of detector, the pixel detector and
142 silicon strip detector. The pixel detector is built from three barrel layers at $r = 44$,
73, 102 mm, and two endcap disks on each side at $z = \pm 345, \pm 465$ mm.

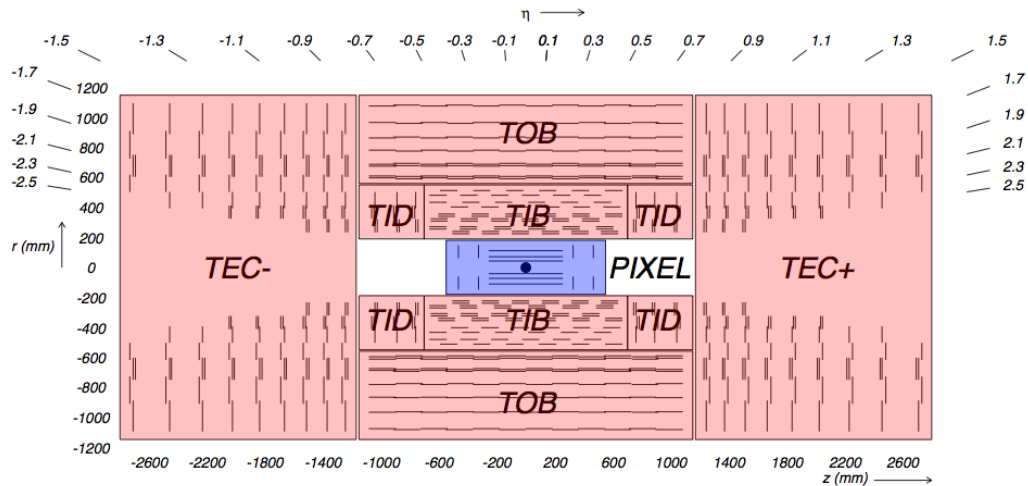


Figure 2-4: Schematic layout of tracker.

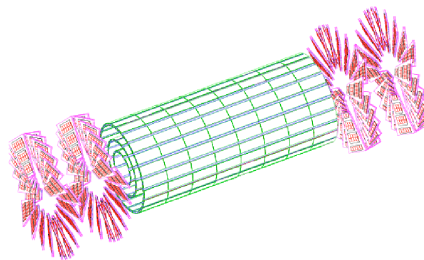


Figure 2-5: The pixel detector inside tracker.

143

144 The pixel detector consists of 1440 segmented silicon sensor modules with total 66 mil-
145 lion readout channels. Charge carriers are distributed over several pixels. The analog

146 pulse height information can be used to calculate the center of certain charge distribution
147 which could improve the hit information. The spatial resolution is measured
148 to be about $10 \mu\text{m}$ for the $r - \phi$ plane or about $20 \mu\text{m}$ for z direction measurement.

149 Outside the pixel detector, there comes the silicon strip detector. The barrel
150 region of silicon strip detector is divided into two parts, the Tracker Inner Barrel
151 (TIB) and the Tracker Outer Barrel (TOB). The former is composed of four layers
152 of silicon sensors with a thickness of $320 \mu\text{m}$ and of strip pitches varying from 80
153 to $120 \mu\text{m}$. The TOB is made of six layers. In this kind of sub-detector, thicker
154 silicon sensors ($500 \mu\text{m}$) are employed, while the strip pitch varies from 120 to 180
155 μm . The endcap region ($|\eta| > 1.6$) is covered by the Tracker Inner Disks (TID)
156 and the Tracker End Cap (TEC). The entire silicon strip detector is comprised of
157 15200 high-sensitivity modules consisting of detecting unit, supporting structure and
158 readout electronic system.

159 2.2.2 ECAL

160 The Electromagnetic Calorimeter (ECAL) measures the energy of photons, electrons
161 and positrons. It it is placed just outside the tracker, but still inside the solenoid.
162 ECAL is made of 74848 lead-tungstate (PbWO_4) crystals. This material is charac-
163 terized by a high density (8.28 g/cm^3), which gives the crystals a very compact form
164 and makes them particularly suitable to be placed inside the magnetic coil. Another
165 reason, this material has also a fast temporal response ($\sim 10 \text{ ns}$) and its radiation
166 length (X_0) of 0.89 cm give ECAL the possibility to fully contain the expansion of
167 the electromagnetic shower.

168 The arrangement of ECAL is shown in Fig. (2-6). The barrel crystals have a front
169 face area of $2.2 \times 2.2 \text{ cm}^2$ and a length of 23 cm. They are positioned at $r = 1.29$
170 m in pseudo-rapidity region $0 < |\eta| < 1.479$. The crystals in the endcaps have a
171 $2.47 \times 2.47 \text{ cm}^2$ front face, a 22 cm length and they are positioned at $z = 3.17 \text{ m}$ in
172 $1.479 < |\eta| < 3.0$. A Preshower detector is placed in front of the endcaps crystals.
173 The active elements of Preshower are two planes of silicon strips with a pitch of 1.9
174 mm, which lie behind disks of lead absorber at depths of $2X_0$ and $3X_0$. It allows the

175 rejection of photon pairs from π^0 decays and improves the estimation of the direction
176 of photons, to enhance the measurement of the two-photon invariant mass.

The energy resolution of the ECAL is given by three different contributions [19]
(E in GeV),

$$\frac{\sigma_E}{E} = \frac{2.8\%}{\sqrt{E}} \oplus \frac{12\%}{E} \oplus 0.3\% \quad (2.1)$$

177 where the first term is statistical in nature, it also contains fluctuation in showering
178 and in the amplification through photodiodes, the second one considers electronic
179 noise and pile-up, the last term is mainly due to the calibration.

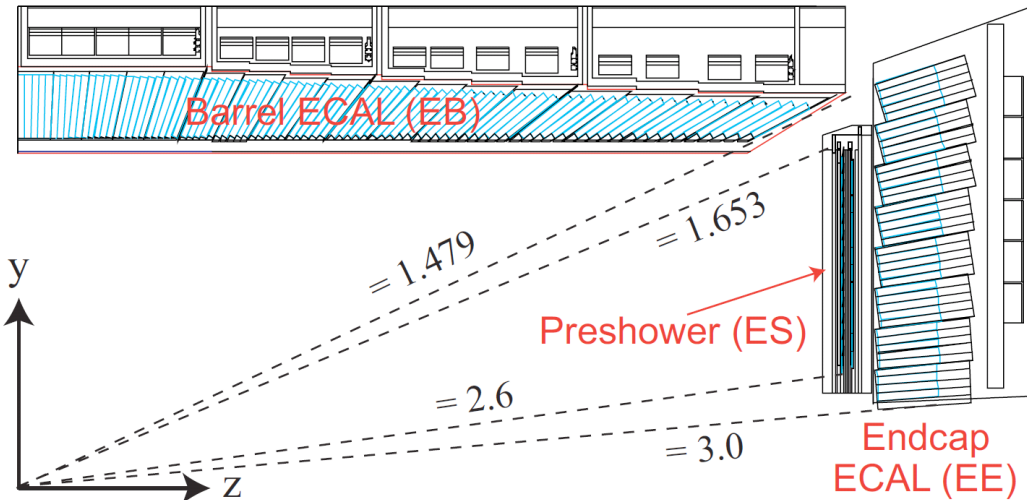


Figure 2-6: Schematic layout of the CMS ECAL.

180 2.2.3 HCAL

181 The hadron calorimeter (HCAL) is placed mainly between ECAL and the magnet
182 coil. It measures the energy of hadrons and mesons. Additionally it provides indirect
183 measurement of the presence of non-interacting, uncharged particles such as neutrinos.
184 The design is strongly influenced by these aims, hence an important requirement is the
185 high hermeticity (the ability to capture every particle emerging from the collisions).
186 This means the detector must cover the biggest possible portion of the solid angle.

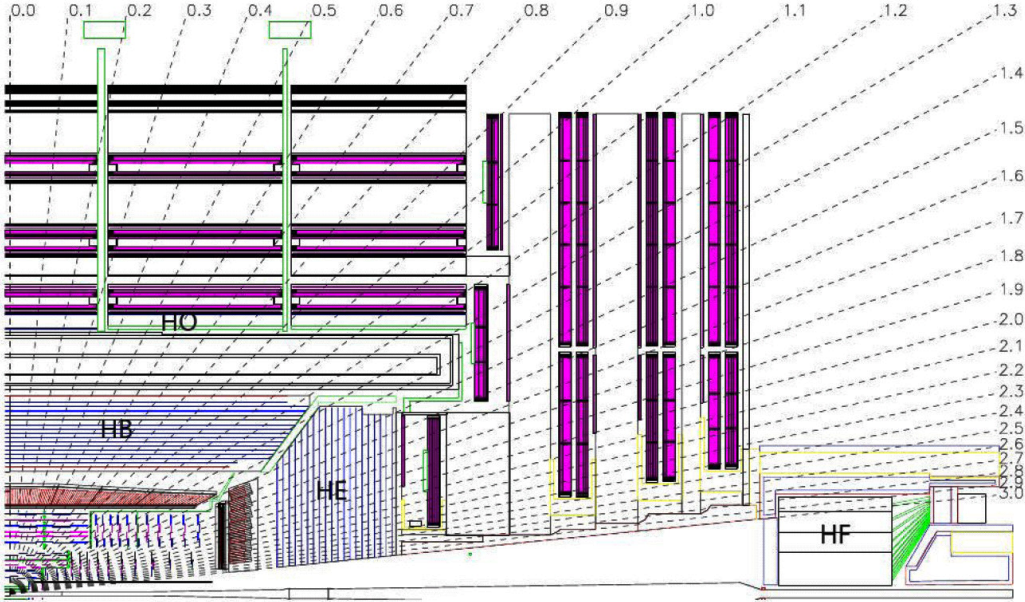


Figure 2-7: Longitudinal view of one quarter of CMS and the location of HB (hadron barrel calorimeter), HE (hadron endcap calorimeter), HF (hadron forward calorimeter) and HO (hadron outer calorimeter)

187 For this reason, a hadron forward calorimeter is required, which is placed outside
 188 the magnet return yokes, with a total coverage of $3 < |\eta| < 5.31$ at 11 m from the
 189 interaction point. Moreover, an outer hadronic calorimeter is placed in the first muon
 190 absorber layer in order to enhance the containment of high energy jets in the central
 191 region of the detector.

192 HCAL is a sampling calorimeter, whose active elements are plastic scintillators
 193 interleaved with brass absorber plates and read out by wavelength shifting fibers.
 194 Brass has been chosen as absorber material for its short interaction length and because
 195 it is non-magnetic. The thickness of the absorber layers is between 60 mm in the barrel
 196 and 80 mm in the endcaps. The barrel has 5.46 interaction lengths at $\eta = 0$ and 10.82
 197 at $\eta = 1.3$, while the endcaps have an average of 11 interaction lengths [20].

The HCAL energy resolution (E in GeV and measured by pion) [21] is

$$\frac{\sigma_E}{E} \simeq \frac{a}{\sqrt{E}} \oplus 5\% \quad (2.2)$$

198 where $a \simeq 65\%$ in the barrel, $a \simeq 85\%$ in the endcaps and $a \simeq 100\%$ in the HF.

199 **2.2.4 Muon Chamber**

200 The efficient detection of muons has primary importance, as muons represent a clear
201 signature for a large number of processes. Muons can penetrate several meters of
202 iron without interacting. Unlike most particles, they are not stopped by any of
203 calorimeters in CMS. Therefore, chambers to detect muons are placed at the very
204 edge of the experiment where they are the only particles likely to register a signal.

205 The muon system fulfills three purposes, muon identification, momentum mea-
206 surement and triggering. Three different types of gaseous detectors are used for CMS
207 muon system depending on the requirements.

208 **Drift Tube**

209 The drift tube (DT) system measures muon positions in the barrel part of the detector.
210 Each DT chamber, on average $2\text{ m} \times 2.5\text{ m}$ in size, consists of 12 aluminium layers,
211 arranged in three groups of four segmentations, each with up to 60 4-cm-wide tubes
212 that contain a stretched wire within each gas volume. The middle group measures
213 the coordinate along the direction parallel to the beam and the two outside groups
214 measure the perpendicular coordinate.

215 **Cathod Strip Chamber**

216 In the two endcaps, where the muon flux and the residual inhomogeneous magnetic
217 field are higher, cathode strip chambers (CSC) are used. CSC is composed of anode
218 wires and cathod strips in the gas volume. The chambers are arranged in 4 disks
219 perpendicular to the beam, and in concentric rings (3 rings in the innermost station,
220 2 in the others) in each of the endcaps.

221 **Resistive Plate Chambers**

222 Resistive plate chambers (RPC) are fast gaseous detectors that provide a muon trigger
223 system parallel with DTs and CSCs. Each RPC consists of two parallel plates, a

²²⁴ positively charged anode and a negatively charged cathode, both made of a very high
²²⁵ resistivity plastic material and separated by a gas volume.

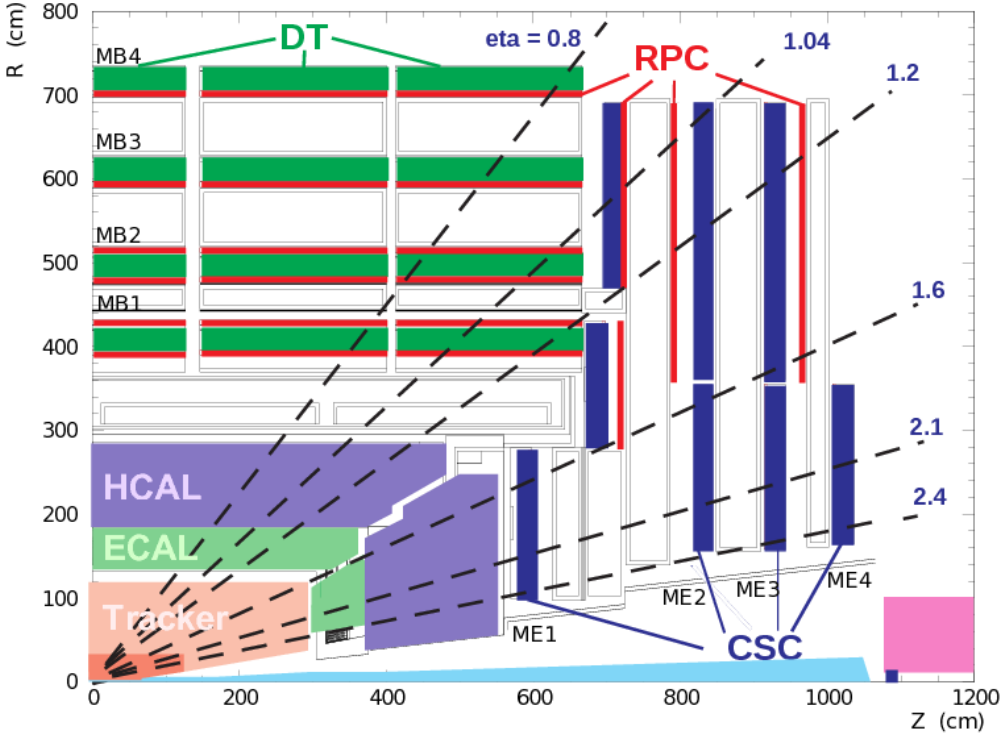


Figure 2-8: Slice view of one quarter of muon chamber system.

²²⁶ 2.2.5 Trigger System

²²⁷ To have a good chance of producing rare particles, a very large number of collisions
²²⁸ is required (LHC proton bunches collide every 25 ns). Most collision events in the
²²⁹ detector are soft and do not produce interesting effects. The amount of data from
²³⁰ each crossing is approximately 1 megabytes, which at the 40 MHz crossing rate would
²³¹ result in 40 terabytes of data a second, an amount that the experiment cannot store.
²³² The task of the trigger system is to reduce the storage rate while keeping a high
²³³ efficiency on the potentially interesting events. In CMS the input rate is reduced in
²³⁴ two steps, Level-1 Trigger (L1T) and High-Level Trigger (HLT).

235 **Level-1 Trigger**

236 After the Level-1 Trigger selection, the event recording frequency is decreased to
237 100kHz [22], which is much smaller than the collision rate. The L1T objects are
238 particles (such as photons, muons and electrons), jet candidates, global transverse
239 energy and missing transverse energy. Level-1 Trigger just choose the event with E_T
240 and P_T higher than the thresholds.

241 **High Level Trigger**

242 High Level Trigger is behind the readout buffers after Level-1 Trigger. It reduces
243 the data output rate to 100Hz by using all the information from CMS including the
244 sub-detectors. The reconstruction algorithms are the same as the off-line analysis.
245 However, the triggering procedure doesn't need maximal precision, therefore these
246 algorithms are modified to be faster even with lower resolution.

247

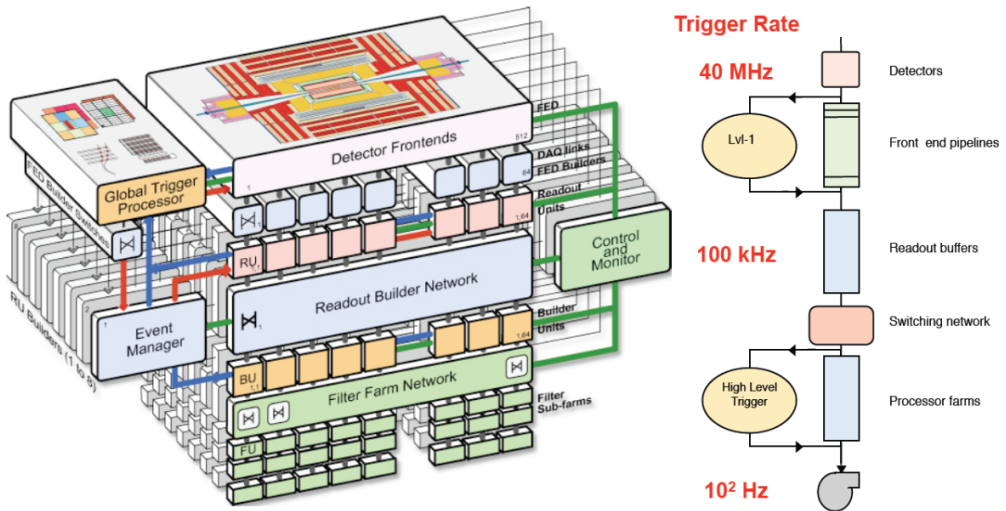


Figure 2-9: CMS triggering and data acquisition architecture.

248 **Chapter 3**

249 **Analysis Procedures**

250 In this chapter, the analysis procedures of the search for Z' decaying into $Z h$ in $llbb$
251 final state are reported. The data sets and Monte Carlo (MC) samples we used in this
252 analysis will be indicated. Physics objects reconstruction and event selections are also
253 introduced. Moreover, background yields and the effects of systematic uncertainties
254 will be demonstrated in the end of this chapter.

255 **3.1 Monte Carlo Samples and Data sets**

256 **3.1.1 Signal MC**

257 As introduced in section 1.2.3, the signal hypothesis is HVT model B benchmark.
258 The heavy resonance (Z') is tested using a wide set of masses from 800 GeV to 2000
259 GeV, one masspoint every 100 GeV (Tab. 3.1).

Sample	Number of events	Cross-section(pb)
ZPrime_ZH_lljj_M800-MADGRAPH	10710	0.00685367
ZPrime_ZH_lljj_M900-MADGRAPH	10209	0.00485861
ZPrime_ZH_lljj_M1000-MADGRAPH	19997	0.003263
ZPrime_ZH_lljj_M1100-MADGRAPH	9370	0.00217483
ZPrime_ZH_lljj_M1200-MADGRAPH	10710	0.00145484
ZPrime_ZH_lljj_M1300-MADGRAPH	9369	0.000979745
ZPrime_ZH_lljj_M1400-MADGRAPH	10497	0.000664783
ZPrime_ZH_lljj_M1500-MADGRAPH	19999	0.000454339
ZPrime_ZH_lljj_M1600-MADGRAPH	8950	0.000312541
ZPrime_ZH_lljj_M1700-MADGRAPH	9369	0.000216282
ZPrime_ZH_lljj_M1800-MADGRAPH	10708	0.000150398
ZPrime_ZH_lljj_M1900-MADGRAPH	10498	0.000105039
ZPrime_ZH_lljj_M2000-MADGRAPH	19999	7.36377e-05

Table 3.1: Signal samples used in the analysis.

Bibliography

- [1] ATLAS Collaboration. Observation of a new particle in the search for the Standard Model Higgs boson with the ATLAS detector at the LHC. *Phys. Lett. B*, 716:1, 2012.
- [2] CMS Collaboration. Observation of a new boson at a mass of 125 GeV with the CMS experiment at the LHC. *Phys. Lett. B*, 716:30, 2012.
- [3] CMS Collaboration. Observation of a new boson with mass near 125 GeV in pp collisions at $\sqrt{s} = 7$ and 8 TeV. *JHEP*, 06:081, 2013.
- [4] CMS Collaboration. Precise determination of the mass of the Higgs boson and tests of compatibility of its couplings with the standard model predictions using proton collisions at 7 and 8 TeV. *Eur. Phys. J. C*, 75:212, 2015.
- [5] ATLAS Collaboration. Measurement of the Higgs boson mass from the $H \rightarrow \gamma\gamma$ and $H \rightarrow ZZ^* \rightarrow 4l$ channels in pp collisions at center-of-mass energies of 7 and 8 TeV with the ATLAS detector. *Phys. Rev. D*, 90:052004, 2014.
- [6] ATLAS Collaboration. Evidence for the spin-0 nature of the Higgs boson using ATLAS data. *Phys. Lett. B*, 726:120, 2013.
- [7] CMS and ATLAS Collaboration. Combined Measurement of the Higgs Boson Mass in pp Collisions at $\sqrt{s} = 7$ and 8 TeV with the ATLAS and CMS Experiments. *Phys. Rev. Lett.*, 114:191803, 2015.
- [8] Mads T. Frandsen. Minimal Walking Technicolor. arXiv:0710.4333 [hep-ph], <http://arxiv.org/abs/0710.4333>, 2007.
- [9] T. Han, H. E. Logan, B. McElrath, and L.-T. Wang. Phenomenology of the little Higgs model. *Phys. Rev. D*, 67:095004, 2003.
- [10] M. Schmaltz and D. Tucker-Smith. LITTLE HIGGS THEORIES. *Annual Review of Nuclear and Particle Science*, 55:no. 1, 229–270, 2005.
- [11] M. Perelstein. Little Higgs models and their phenomenology. *Progress in Particle and Nuclear Physics*, 58:no. 1, 247–291, 2007.
- [12] R. Contino, D. Pappadopulo, D. Marzocca, and R. Rattazzi. On the effect of resonances in composite Higgs phenomenology. *Journal of High Energy Physics*, 2011:no. 10, 1–50, 2011.

- 290 [13] D. Marzocca, M. Serone, and J. Shu. General composite Higgs model. *Journal*
291 *of High Energy Physics*, 2012:no. 8, 1–52, 2012.
- 292 [14] B. Bellazzini, C. Csaki, and J. Serra. Composite Higgses. *Eur. Phys. J.*, C74:no.
293 5, 2766, 2014.
- 294 [15] D. Pappadopulo, R. Torre A. Thamm, and A. Wulzer. Heavy vector triplets:
295 bridging theory and data. *Journal of High Energy Physics*, 2014:no. 9, 1–50,
296 2014.
- 297 [16] Andrea Wulzer. An Equivalent Gauge and the Equivalence Theorem.
298 arXiv:1309.6055 [hep-ph], <http://arxiv.org/abs/1309.6055>, 2013.
- 299 [17] V. Barger, W.-Y. Keung, and E. Ma. Gauge model with light W and Z bosons.
300 *Phys. Rev. D*, 22:727, 1980.
- 301 [18] Lisa Benato, Yu-Hsiang Chang, Ching-Wei Chen, Michele de Gruttola, Ra-
302 man Khurana Ji-Kong Huang, Stefano Lacaprara, Yun-Ju Lu, Jacopo Pazzini,
303 Maurizio Pierini, Henry Yee-Shian Tong, Jun-Yi Wu, Shin-Shan Eiko Yu, Marco
304 Zanetti, and Alberto Zucchetta. Search for heavy resonances decaying into a vec-
305 tor boson and a higgs boson in the $(ll, l\nu, \nu\nu)b\bar{b}$ final state. CMS Note 2015/186,
306 CMS, 2015.
- 307 [19] A. Benaglia. The CMS ECAL performance with examples. *JINST*, 09:C02008,
308 2014.
- 309 [20] CMS HCAL Collaboration. Design, performance, and calibration of cms hadron-
310 barrel calorimeter wedges. CMS Note 2006/138, CMS, 2006.
- 311 [21] Victor Daniel Elvira. Measurement of the pion energy response and resolution
312 in the cms hcal test beam 2002 experiment. CMS Note 2004/020, CMS, 2004.
- 313 [22] J. Brooke on behalf of the CMS Collaboration. Performance of the CMS Level-1
314 Trigger. arXiv:1302.2469 [hep-ex], <http://arxiv.org/abs/1302.2469>, 2013.